Cite this: *Dalton Trans.*, 2024, **53**, 6234

White light-emitting ZnO:Dy³⁺ nanophosphors: delving into the spectroscopic parameters via Judd–Ofelt analysis†

Rajendran Raji,^a Gopalakrishnan Jyothi,^c Sajesh Sasidharan^a and Kunnel Gopalan Gopchandran^{id} *^b

Developing a single-phase white emitting nanophosphor with high quantum efficiency has become a hotspot for scientific world. Herein, single-phase white-light emitting Zn_{1-x}O:xDy³⁺ nanophosphors have been synthesized via a sonochemical method. X-ray diffraction analysis and Raman spectroscopy-based investigations confirmed the hexagonal wurtzite phase for Zn_{1-x}O:xDy³⁺ nanophosphors with preferential growth along the (101) plane. Scanning electron microscopy images showed the formation of a ribbon-shaped morphology with a diameter of ~25 nm. The emission spectra of the Dy³⁺-activated ZnO nanophosphors exhibited three distinct peaks, namely blue (480 nm), yellow (572 nm), and red (635 nm) emissions, under near-UV excitations related to the ⁴F_{9/2} → ⁶H_J (J = 15/2, 13/2, and 11/2) transitions of Dy³⁺ ions. The values of CIE chromaticity coordinates for the optimized phosphor (x = 0.329, y = 0.334) with correlated color temperature (CCT) of 5657 K indicated cool white-light emission from the phosphor. The thermal stability of ZnO:Dy³⁺ nanophosphors was probed by temperature-dependent luminescence. Quantitative evaluation of Judd–Ofelt intensity parameters, radiative parameters, luminescence decay, and quantum efficiency of Zn_{1-x}O:xDy³⁺ using the J–O theory suggests that these nanophosphors are promising luminescent media for commercial white LEDs and other display devices.

Received 5th December 2023,
Accepted 29th February 2024

DOI: 10.1039/d3dt04070d

rsc.li/dalton

1. Introduction

As the hotspot in the solid-state lighting area, the development of highly power efficient, sustainably devised solid-state lighting devices is a key concern for materials scientists and researchers globally as the world is now experiencing an energy crisis.^{1–3} Solid-state lighting technology, especially white light-emitting diodes (WLEDs), has completely revolutionized the field of luminescence owing to its exceptional properties, which include low power consumption, high energy efficacy, long lifetime, excellent lumen performance, and environmental stewardship.^{1,3–5}

Trivalent lanthanide (Ln³⁺)-activated inorganic phosphors have attracted considerable attention as next-generation lighting sources due to their superior physicochemical features such as long-lived luminescence, narrow emission bands, appropriate color rendering index (CRI) and correlated color

temperature (CCT) and low toxicity.^{3,5–7} The intricate luminescence properties of Ln³⁺ ions arise from their unique electronic structure that enables Ln³⁺ ions in solids to efficiently emit photons in the ultraviolet to visible or infrared (IR) spectral regions.^{3,7} Among the various down-shifting lanthanide-based activators, Dy³⁺ ions are a potential candidate for producing white light owing to their inner-shell 4f–4f transitions, especially ⁴F_{9/2} → ⁶H_{15/2}, magnetic and ⁴F_{9/2} → ⁶H_{13/2}, electric dipole transitions, resulting in blue and yellow emission, respectively. The intensity of yellow emission is very sensitive to the host matrix, and therefore, the suitable selection of the host matrix for Dy³⁺ is crucial, which affects the energy transfer and emission characteristics of the phosphor.^{3–7}

In this context, zinc oxide (ZnO), an efficient oxide-based semiconductor, has attracted much attention from the scientific fraternity because of its unique optoelectronic properties, mainly its direct wide band gap (~3.37 eV), large exciton binding energy (~60 meV) and broad absorption band in the near-UV region at room temperature.^{8–10} Moreover, ZnO exhibits a broad emission spectrum from the UV to the red spectral region. The emission band in the UV region originates from free exciton recombination and the broad emission band in the visible region originates from different kinds of inherent defects such as oxygen vacancies (Vo), oxygen interstitials (Oi),

^aDepartment of Physics, Sree Narayana College, Sivagiri, Varkala, 695145, India^bDepartment of Optoelectronics, University of Kerala, Thiruvananthapuram, 695581, India. E-mail: gopchandran@yahoo.com^cDepartment of Physics, M.S.M. College, Kayamkulam, 690502, India† Electronic supplementary information (ESI) available. See DOI: <https://doi.org/10.1039/d3dt04070d>

oxygen antisites (ZnO), zinc vacancies (Vzn), zinc interstitials (Zni) and zinc antisites (OZn).^{11–14} Recent studies showed that the luminescence efficiency and transition probabilities of ZnO can be tuned by tailoring the band structure *via* elemental doping.¹² The doping of suitable trivalent RE activators into ZnO having various vacancies and defects offers enhanced luminescence characteristics through the effective non-radiative transition from ZnO to rare-earth dopants.^{14,15}

Moreover, doping of Dy³⁺ ions into the ZnO lattice can augment emission in the visible and near-infrared region due to the excitation of charge carriers in the energy levels of Dy³⁺ ions with the aid of resonant energy transfer from the ZnO matrix.^{9–11} Recently, Bindhu *et al.*¹⁶ reported the development of a dual-emitting Dy³⁺-activated Sr₂NaMg₂V₃O₁₂ phosphor for multifunctional applications in solid-state lighting and optical thermometry. Vasudevan *et al.*¹⁷ studied the radiative properties of green-synthesized ZnO:Dy³⁺ nanophosphors by the Judd–Ofelt theory and reported the potential application of these phosphors in bluish white light NUV-LEDs. Yuan *et al.*¹⁸ reported the synthesis of a blue-light-excited cyan phosphor by co-doping Bi³⁺ into Ce³⁺-activated BaLu₂Al₂Ga₂SiO₁₂. The synthesis of zero-dimensional Cs₃ScCl₆:Sb₃₊(CSC:Sb³⁺) nanocrystals with bright white-light emission was reported by Samanta *et al.*,¹⁹ which was a result of the combination of the excessive blue and yellow emissions of carbon dots and spin-forbidden electronic transitions of Sb³⁺ ions. Dutta *et al.*²⁰ studied the luminescence and radiative properties of Dy³⁺-doped CaMoO₄ phosphors and reported the suitability of this phosphor as an efficient luminescent medium for light-emitting devices. Thus, it is time to comprehensively study the photoluminescence properties and emission tunability of Dy³⁺-activated ZnO nanophosphors for multifunctional applications.

In the present work, a series of Dy³⁺-activated ZnO nanophosphors have been prepared by sonochemical method and attempts were made to explore their potential as phosphors for white LEDs by detailed photoluminescence and colorimetric analysis. Also, attempts were made to estimate spectral parameters, luminescence decay time, and quantum yields of the Dy³⁺-doped ZnO nanophosphors using Judd–Ofelt theory from the excitation spectra. The stimulated-emission cross-sections along with the spectroscopic quality factors estimated from emission spectra demonstrated the potential of this phosphor for use in optical devices.

2. Experimental section

2.1 Synthesis

Materials used for synthesis were zinc nitrate hexahydrate (Zn(NO₃)₂·6H₂O, 99.98%, Sigma-Aldrich), dysprosium trinitrate hydrate (Dy(NO₃)₃·xH₂O, 99.9%, Sigma-Aldrich) and sodium hydroxide (NaOH, 98%, Sigma-Aldrich).

ZnO:xDy³⁺ nanoparticles with varying concentrations of Dy³⁺ ($x = 0, 0.04, 0.08, 0.12, 0.16, \text{ and } 0.20$ at%) were synthesized by the co-precipitation method assisted by ultrasound

radiation. This method contains two steps. In the first step, zinc nitrate hexahydrate and 0.04 at% Dy(NO₃)₃·xH₂O were separately dissolved in 20 mL and 5 mL of deionized water by using a conventional ultrasound bath for 7 minutes. Next, 1.2 M of NaOH was dissolved in 20 mL of deionized water using an ultrasound bath for 10 min. In the second step, the two nitrate solutions were mixed under vigorous stirring at room temperature for 10 minutes to ensure uniform mixing, and the aqueous solution of NaOH was added slowly, yielding a white precipitate. The reaction was allowed to proceed for 10 min after the complete addition of NaOH. The resulting white suspension was exposed to ultrasonic radiation for 30 minutes. The resulting mixture was centrifuged to remove the solvent. The obtained samples were washed thrice using distilled water and ethanol to remove the by-products generated during the synthesis process. Finally, the obtained powdery substances were fully ground and then subjected to annealing in a muffle furnace at 300 °C for 2 h to obtain ZnO:Dy³⁺ nanoparticles.

2.2 Characterization

The structural and phase purity analysis of the ZnO:Dy³⁺ nanophosphors were examined using an X-ray diffractometer (Bruker D8 ADVANCE having Cu-K α radiation, $\lambda = 1.5405$ Å) in the angular range of 2θ from 20 to 80°. The morphology determination, X-ray dot mapping imaging, and elemental analysis were carried out using a Nova Nano SEM-450 Field Emission Scanning Electron Microscope equipped with an XFlash detector 6/10 (Bruker) and using the software QUANTA X 200. The elemental analysis was further carried out using Inductively coupled Plasma Mass Spectrometry (Thermo Scientific iCAP Qc ICP-MS). The vibrational analysis of the samples was performed using a Horiba Jobin–Yvon LABRAM-HR800 confocal laser micro-Raman spectrometer with an excitation radiation of wavelength 514.5 nm from an argon ion laser and a Peltier-cooled CCD detector. The chemical states of Dy in the samples were identified using a Krato analytical photoelectron spectrometer with monochromatic Al K α radiation (1486 eV) as the excitation source. The diffuse reflectance (DRS) spectra of all the samples were recorded using a JascoV550 UV-visible spectrophotometer attached with an integrating sphere (ISV-469) attachment for DRS measurement. Room temperature photoluminescence spectra were obtained with a Spectrofluorimeter (Horiba Jobin Yvon Fluorolog III) and the lifetime measurements were recorded using a phosphorimeter attached to the spectrofluorometer (Spex-Fluorolog DM-3000F). The temperature-dependent photoluminescence measurements in the 80–500 K range were carried out using an FLS 1000 spectrophotometer Edinburgh Instruments with an Optistat cryostat by Oxford Instruments.

3. Results and discussion

3.1 Crystal structure, morphology, and composition analysis

The crystal structure and phase purity of Dy³⁺-activated ZnO nanostructures were analyzed using XRD patterns. Fig. 1 illus-

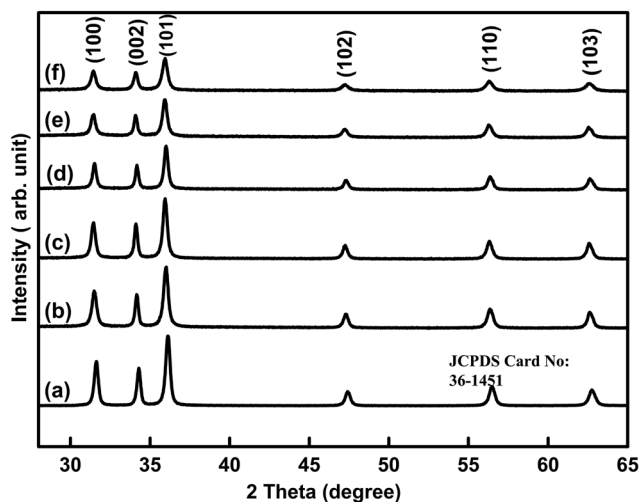


Fig. 1 XRD patterns of ZnO:Dy³⁺ nanophosphors with Dy³⁺ doping levels of (a) 0, (b) 0.04, (c) 0.08, (d) 0.12 (e) 0.16 and (f) 0.2 at%.

trates the X-ray diffraction patterns of Zn_{1-x}O:xDy³⁺ ($x = 0, 0.04, 0.08, 0.12, 0.16$ and 0.2) nanophosphors, indexed to the hexagonal wurtzite phase of ZnO (JCPDS Card No: 36-1451, space group: $P6_3mc$, $a = 3.2498$ Å, $c = 5.2066$ Å), with preferential growth along the (101) crystal plane. No other traces of impurity or secondary phase of Dy³⁺ were detected, confirming the single-phase nature of the ZnO:Dy³⁺ nanostructure, and it also indicates the incorporation of the Dy³⁺ ions into the Zn²⁺ lattice sites by substitution rather than at interstitial positions.

The intensity of the diffraction peaks was found to decrease and their full width at half maximum increase with Dy³⁺ content, which indicates the replacement of Zn²⁺ sites by the Dy³⁺ ions.¹⁴ In addition, a small shift in the position of the preferentially oriented crystal plane (101) towards the lower angle (2θ) side was observed as a result of the incorporation of Dy³⁺ ions at the cation sites (Fig. S1†). Almessiere *et al.*²¹ reported a similar shift in the position of diffraction peaks towards the lower angle side and suggested that the substitution of Zn²⁺ sites by the Dy³⁺ dopant would cause a charge compensation due to the valence difference between the cation sites and the dopant, leading to a distortion in the crystal and hence strain in the lattice. Moreover, the ionic radii difference between Zn²⁺ ions (CN = 4, 0.74 Å) and Dy³⁺ (CN = 4,

0.91 Å) ions was 0.017 Å, which is very close to the substitution sites for Dy³⁺ dopant sites; these aspects clearly illustrate the possibility of the substitutional incorporation of Dy³⁺ ions at Zn²⁺ sites of the ZnO lattice.^{22,23}

The average crystallite size (D) of these nanostructures was determined from the most prominent peaks (100), (101) and (002) of XRD data using the Scherrer formula:²⁴

$$D = \frac{0.9\lambda}{\beta \cos \theta} \quad (1)$$

where λ is the wavelength (Cu K α) of the X-ray radiation used, θ is the Bragg angle and β is the full-width at half-maximum (FWHM) corresponding to the most prominent peak (100) (101) and (002) measured in radians.

A monotonic decrease in the crystallite size from 28 to 20 nm was observed with Dy³⁺ content and is probably associated with the hindered growth of crystallites due to the substitution of Dy³⁺ ions with a larger ionic radius than Zn²⁺ ions.²¹ The study of the lattice parameters a and c of the ZnO:Dy³⁺ nanostructures indicates that the Dy³⁺ ion incorporation promotes the expansion of the lattice as evidenced by an increase in the unit cell parameters (Table 1), which again confirmed the possibility of incorporation of the Dy³⁺ ions as a substituent at the Zn²⁺ site in the hexagonal ZnO lattice.^{22,23} The observed slight peak shift towards the lower angle side, broadening of the peaks, decrease in crystallite size, and larger lattice constants as compared with those of pure ZnO indicate the presence of micro-strain (ϵ) in the samples. The micro-strain (ϵ) associated with the ZnO:Dy³⁺ nanostructures can be calculated using the following relation:²⁵

$$\text{Micro-strain } (\epsilon) = \frac{\beta \cos \theta}{4}. \quad (2)$$

The observed slight increase of lattice strain on doping is also considered to be a further indication of substitutional incorporation.²⁵

Fig. 2(a and b) shows typical FE-SEM images of ZnO and ZnO:0.16Dy³⁺ nanophosphors and both samples exhibit a ribbon-shaped morphology with an average diameter of about 24 nm for ZnO and 20 nm for ZnO:0.16Dy³⁺ nanophosphors, respectively. Also, ZnO nanoribbons possess well-defined boundaries with less agglomeration, whereas the incorporation of Dy into the ZnO lattice leads to the aggregation of

Table 1 Structural and optical properties of the synthesized ZnO:Dy³⁺ nanophosphors [for bulk ZnO $a = b = 0.3249$ nm, $c = 0.5206$ nm (JCPDS 36-1451)]

Dy content (at%)	FWHM (°)	Crystallite size D_{hkl} (nm)	Lattice parameter		Strain ϵ	Band gap(eV)
			a (nm)	c (nm)		
0	0.2772	30	0.3252	0.5215	0.0177	3.25
0.04	0.2910	28	0.3255	0.5225	0.0192	3.26
0.08	0.3171	26	0.3258	0.5228	0.0201	3.27
0.12	0.3250	25	0.3261	0.5225	0.0261	3.29
0.16	0.4013	20	0.3265	0.5232	0.0307	3.31
0.20	0.3476	24	0.3257	0.5235	0.0338	3.30

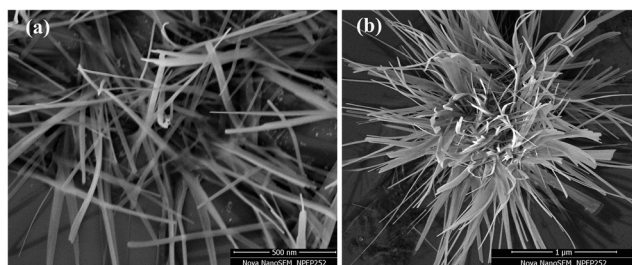


Fig. 2 FE-SEM images of (a) ZnO and (b) ZnO:Dy³⁺ (0.16 at%) nanophosphors.

nanoribbon structures. ZnO:0.16Dy³⁺ nanophosphors maintained the ribbon-shaped morphology, suggesting that Dy doping had little influence on the alteration of the morphology of the nanoparticles in the present case.

The elemental analysis of ZnO:Dy³⁺ nanostructures was performed using energy dispersive X-ray (EDX) spectroscopy and is given in Fig. 3(e and f). The quantitative EDX and ICP-MS analyses of the nanophosphors (Table 2) indicate that the concentrations of elements are identical to the theoretical stoichiometry. The elemental X-ray dot mapping images (Fig. 3(a–d)) showed that the constituent elements were uniformly dispersed in the samples.

Micro-Raman spectroscopy is an excellent tool for understanding the structural modification and surface-related

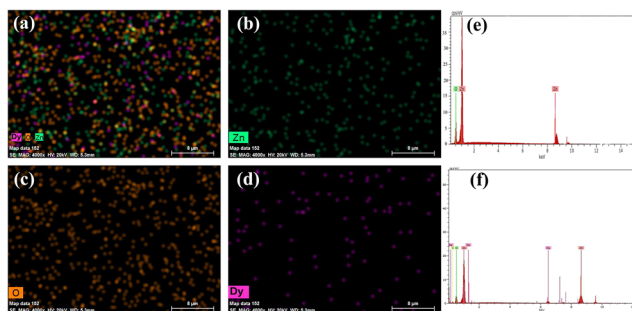


Fig. 3 (a–d) Elemental X-ray dot mapping images ZnO:Dy³⁺ nanophosphors and (e–f) EDX spectra of ZnO and ZnO:Dy³⁺ (0.16 at%) nanophosphors.

Table 2 Atomic percentage of elements obtained from EDX analysis

Dy doping concentration (at%)	Elemental composition from EDX (at%)			Dy content as per ICP-MS analysis (at%)
	Zn	O	Dy	
0	50	50	0	0
0.04	49.98	49.98	0.032	0.036
0.08	49.97	49.96	0.074	0.078
0.12	49.95	49.95	0.10	0.11
0.16	49.94	49.93	0.13	0.14
0.20	49.92	49.92	0.16	0.18

defects of the crystal. There are nine optical modes for the hexagonal wurtzite phase of ZnO with C_{6v} symmetry predicted by factor group theory,^{26–29} given by the following:

$$\Gamma_{\text{optical}} = A_1(\text{R, R}) + 2B_1 + E_1(\text{IR, R}) + 2E_2(\text{R}) \quad (3)$$

A_1 and E_2 modes are polar and are active in both Raman and IR regions and the B_1 modes are silent modes; the E_2 modes are non-polar and Raman-active only.^{27,28} Due to the microscopic electric field associated with the LO phonons, the A_1 and E_1 modes split into transverse optical (A_{1T} & E_{1T}) and longitudinal optical (A_{1L} & E_{1L}) phonons with different frequencies. Also, the E_2 mode was split into E_2 (high) and E_2 (low) modes.^{27–29}

Fig. 4 represents the Raman spectra of ZnO:Dy³⁺ nanophosphors over the spectral range 50–1300 cm^{-1} . The Raman spectra of undoped and Dy-doped ZnO nanophosphors exhibited almost similar patterns. All the samples show an intense Raman band at $\sim 100 \text{ cm}^{-1}$, corresponding to the E_2 (low) mode, due to the vibration of the Zn sublattice. The appearance of an intense peak at 438 cm^{-1} corresponds to E_2 (high) mode, due to the vibration of oxygen atoms. These two non-polar modes are a characteristic feature of the wurtzite phase of ZnO.^{28,29} It is evident from the Raman spectra that Dy³⁺ ion doping significantly influences the different vibrational modes of ZnO. The E_2 (high) mode shows a systematic shift to lower wavenumbers (438 to 433 cm^{-1}) with Dy³⁺ content, indicating the incorporation of Dy³⁺ ions into Zn²⁺ sites and the formation of Dy³⁺-induced defects in the ZnO lattice.³⁰ In addition, the intensity of the E_1 (LO) mode ($\sim 580 \text{ cm}^{-1}$) varies with Dy doping, meaning that the introduction of Dy³⁺ induces defects such as zinc interstitials, and oxygen vacancies in the crystal without altering the crystal structure.^{30,31} Moreover, the observed increase in the ratio of the intensity of E_2 (high) mode to E_1 (LO) mode indicates the preservation of the wurtzite phase with good crystalline nature.^{31,32}

The chemical configuration and bonding states of Dy³⁺ in ZnO:Dy³⁺ nanophosphors were further explored with X-ray

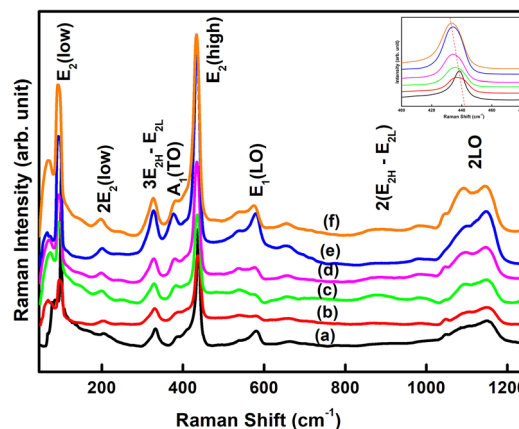


Fig. 4 Micro-Raman spectra of ZnO:Dy³⁺ nanophosphors with varying Dy³⁺ doping levels: (a) 0, (b) 0.04, (c) 0.08, (d) 0.12, (e) 0.16 and (f) 0.2 at%. [Inset: shift of the E_2 (high) mode].

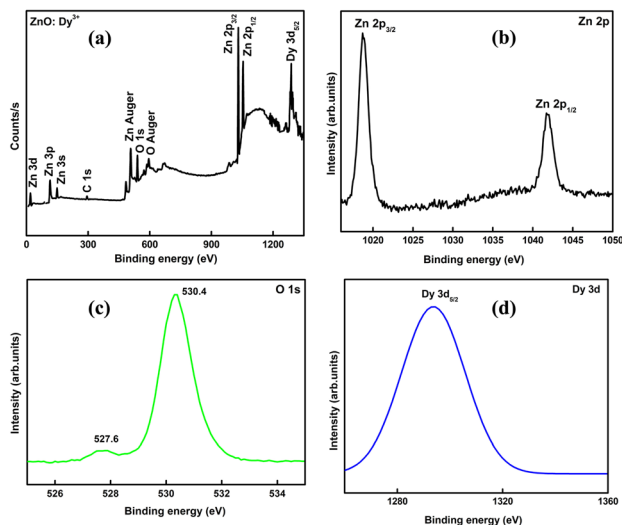


Fig. 5 XPS spectra of ZnO:Dy³⁺ (0.16 at%) nanophosphors: (a) survey scan spectrum; (b) Zn 2p; (c) O 1s and (d) Dy 3d.

photoelectron spectroscopy and are shown in Fig. 5(a and d). The XPS survey scan clearly shows the core level of Zn (2p, 3p, 3d, and 3s), O (1s), Dy (3d), and C (1s), confirming the high purity of the samples. The high-resolution XPS spectrum of Zn 2p is composed of two symmetric peaks corresponding to Zn 2p_{3/2} and Zn 2p_{1/2} states with binding energies of 1018.6 and 1041.7 eV, respectively.³² The binding energy difference between Zn 2p_{3/2} and Zn 2p_{1/2} is 23.1 eV, which is consistent with the standard reference of 22.97 eV and can be due to the spin-orbit splitting of the Zn²⁺ valence state.³² The O 1s core level spectrum displayed in Fig. 5(c) shows a broad spectrum with a shoulder peak, centered at 527.6 and 530.4 eV, suggesting the existence of two different kinds of O species in the sample. The first peak at 527.6 eV can be attributed to O²⁻ ions that are surrounded by Zn atoms in the hexagonal structure of ZnO. The highly intense peak at 530.4 eV can be assigned to O²⁻ ions that are in oxygen-deficient regions and the surface hydroxyl groups.^{25,32,33} The core level XPS spectrum of Dy displayed a broad peak at around 1294 eV and can be assigned to the Dy 3d_{5/2} state, which is relatively close to the values reported for Dy(III) oxides.^{28, 33–35}

3.2 Optical studies

3.2.1 Diffuse reflectance spectra and bandgap. The diffuse reflectance spectra of ZnO:xDy³⁺ nanostructures ($x = 0, 0.04, 0.08, 0.12, 0.16,$ and 0.20 at%) are shown in Fig. 6. A broad excitonic absorption band in the UV region (~ 378 nm) was observed and attributed to the electron transition from the valence band to the conduction band (O_{2p} → Zn_{3d} state). NIR absorption bands at 753 and 804 nm were also observed due to ⁶H_{15/2} → ⁶F_{3/2} and ⁶H_{15/2} → ⁶F_{5/2} transitions of Dy³⁺ ions, respectively.¹⁶

The optical bandgaps of ZnO:Dy³⁺ nanostructures were calculated using the Kubelka–Munk method from the diffuse reflectance spectra. The Kubelka–Munk function $F(R_\infty)$,

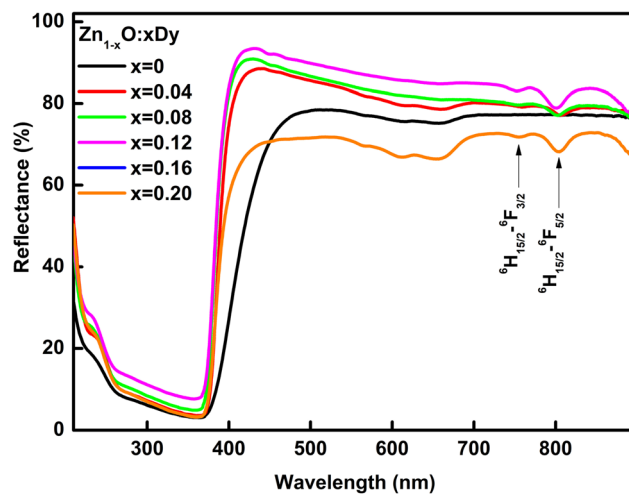


Fig. 6 Diffuse reflectance spectra of ZnO:Dy³⁺ nanostructures with ¹⁵Dy³⁺ doping levels (0.04–0.2 at%).

absorption coefficient (K) and scattering coefficient (S) are related by the following equation:^{34,36}

$$F(R_\infty) = \frac{(1 - R_\infty)^2}{2R_\infty} = \frac{K}{S} \quad (4)$$

where $F(R_\infty)$ is the Kubelka–Munk function, $R_\infty = R_{\text{sample}}/R_{\text{standard}}$, is the diffuse reflectance of the sample with respect to the BaSO₄ reference.

Since ZnO is a direct band gap material, the relation connecting the absorption coefficient (α) and band gap energy (E_g) can be written as follows:³⁷

$$\alpha(h\nu) = B(h\nu - E_g)^{1/2} \quad (5)$$

where B is a constant. The band gap energies of the samples were determined by plotting the variation of the Kubelka–Munk function with photon energy according to the following relation:

$$(F(R_\infty)h\nu)^2 \propto (h\nu - E_g) \quad (6)$$

From the $(F(R_\infty)h\nu)^2$ versus photon energy ($h\nu$) plot, the band gap energy was determined by extrapolating the linear part of the $(F(R_\infty)h\nu)^2$ curve to zero (Fig. 7).³² The observed systematic increase in optical band gap energy (Table 1) may be due to the incorporation of Dy³⁺ ions into the ZnO lattice and is attributed to the Brustein–Moss (BM) effect.³⁸ The incorporation of Dy³⁺ ions improves the electron carrier concentration within the conduction band, which causes the lifting of the Fermi level in the conduction band and results in an increase in the effective band gap.^{38–40} Amira *et al.*³¹ reported a similar broadening of the band gap with Dy³⁺ doping and ascribed it to the Brustein–Moss shift, which results from the filling of the conduction band of n-type materials or the valence band of p-type materials.

3.2.2 Photoluminescence properties of Zn_{1-x}O:xDy³⁺ nanophosphors. The photoluminescence excitation spectra of

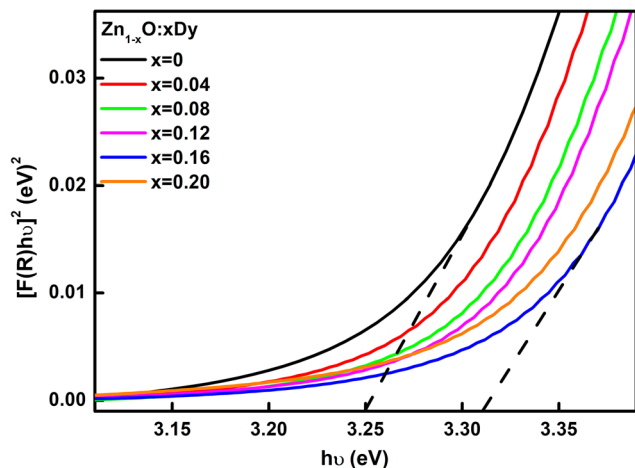


Fig. 7 Kubelka–Munk plots of ZnO:Dy³⁺ nanophosphors with varying Dy³⁺ doping levels (0–0.2 at%).

Zn_{1-x}O:xDy³⁺ ($x = 0, 0.04, 0.08, 0.12, 0.16, \text{ and } 0.20$ at%) nanophosphors monitored with the emission wavelength of 572 nm are given in Fig. 8. The peaks observed in the spectra arise from the electronic transitions, ${}^6\text{H}_{15/2} \rightarrow {}^6\text{P}_{3/2}$ (318 nm) ${}^6\text{H}_{15/2} \rightarrow {}^6\text{P}_{7/2}$ (352 nm), ${}^6\text{H}_{15/2} \rightarrow {}^6\text{P}_{5/2}$ (366 nm), ${}^6\text{H}_{15/2} \rightarrow {}^4\text{I}_{13/2}$ (388 nm), ${}^6\text{H}_{15/2} \rightarrow {}^4\text{G}_{11/2}$ (427 nm), ${}^6\text{H}_{15/2} \rightarrow {}^4\text{I}_{15/2}$ (452 nm) and ${}^6\text{H}_{15/2} \rightarrow {}^4\text{F}_{9/2}$ (476 nm) of Dy³⁺ ions. The spectra revealed that these phosphors can be excited at 366, 388, and 450 nm.^{34,41–43}

The emission spectra of Dy³⁺-activated ZnO nanophosphors under 388 nm excitation (Fig. 9) exhibit three distinct peaks at 480, 572 and 635 nm and are related to the $f \rightarrow f$ electronic transitions of Dy³⁺ ions, ${}^4\text{F}_{9/2} \rightarrow {}^6\text{H}_{15/2}$, ${}^4\text{F}_{9/2} \rightarrow {}^6\text{H}_{13/2}$ and ${}^4\text{F}_{9/2} \rightarrow {}^6\text{H}_{11/2}$, respectively.⁴³ The blue emission peak at ~480 nm can be assigned to the magnetic dipole (MD) allowed transition, which is less sensitive to the local site symmetry, whereas the yellow emission peak at ~572 nm can be attributed to the electric dipole (ED) allowed transition and is hyper-

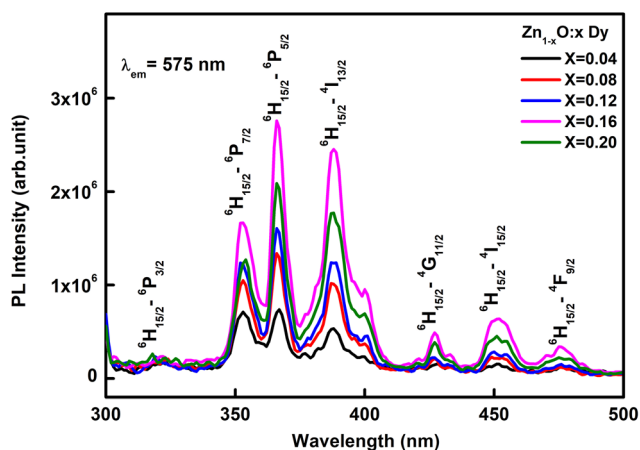


Fig. 8 The PLE spectra of ZnO:Dy³⁺ nanophosphors with varying Dy content (0.04–0.2 at%) monitored under an emission of 574 nm.

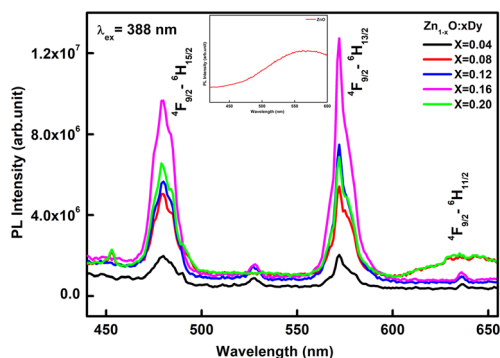


Fig. 9 Emission spectra of ZnO:Dy³⁺ nanophosphors prepared with different Dy³⁺ doping levels (0.04–0.2 at%) (Inset shows emission spectra of ZnO).

sensitive to the local site symmetry or site preference of Dy³⁺ ions in the crystal lattice.^{16,43} The observed dominance of electric dipole transitions over magnetic dipole transitions suggests that Dy³⁺ ions are located in a highly distorted environment with minimal crystal field symmetry. The asymmetric ratio of ZnO:Dy³⁺ nanophosphors was evaluated to understand the site symmetry or distortion of the crystal site around the Dy³⁺ ions and was found to increase with Dy³⁺ content up to 0.16 at% and then decrease. From Table 4, the observed high value of the asymmetric ratio indicates that the Dy³⁺ ions prefer to occupy a low symmetry site without an inversion center.^{42,43} Apart from intense blue and yellow bands, a kenspeckle red emission band was also present at ~635 nm due to the ${}^4\text{F}_{9/2} \rightarrow {}^6\text{H}_{11/2}$ transition. The inset of Fig. 9 shows the emission spectra of ZnO nanoparticles due to near-UV excitation (388 nm) and it exhibits a broad visible emission centered at ~582 nm, due to the presence of oxygen interstitials located at 2.14 eV below the conduction band.^{9–11} A schematic illustration of the main transitions of ZnO:Dy³⁺ nanophosphors is shown in the energy level diagram (Fig. 10). It was observed that the integrated emission intensity was enhanced and the asymmetric ratio increased from 1.06 to 1.37 for optimum Dy³⁺ content (0.16 at%) in the present work (Fig. S2[†]); beyond that, luminescence quenching occurs. The observed quenching of emission intensity at higher concentrations can be attributed to non-radiative energy transfer between activator ions due to the shortened interionic distance between Dy³⁺ ions. The critical distance, R_c , for effective energy transfer between Dy³⁺ ions is given by Blasse:⁴⁴

$$R_c = 2 \left[\frac{3V}{4\pi N X_c} \right]^{1/3} \quad (7)$$

where V is the unit cell volume (49.9 Å³ for ZnO), N is the number of cation sites in the unit cell ($N = 4$ for hexagonal ZnO) and X_c is the critical ion concentration. Earlier studies proposed that two energy transfer mechanisms were responsible for the concentration quenching, namely, the exchange interaction (for $R_c < 5$ Å), and multipole interactions (for $R_c > 5$ Å). The calculated R_c value was 15.5 Å, which effectively rules

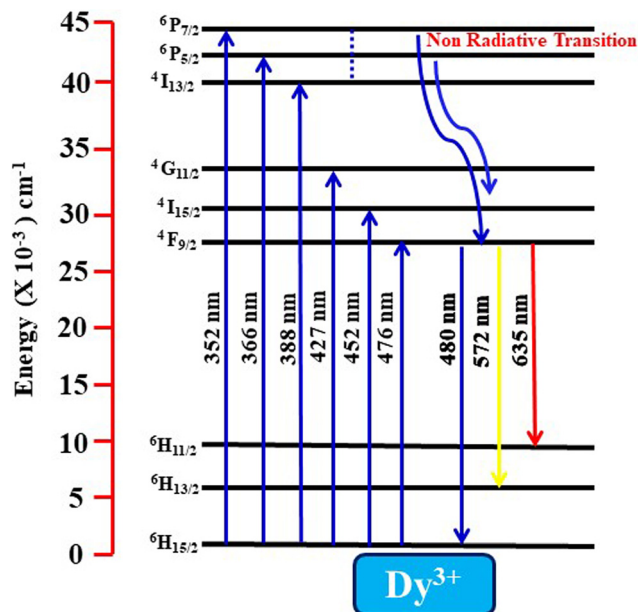


Fig. 10 A schematic model corresponding to emissions from ZnO:Dy³⁺ nanophosphors.

out the possibility of electrostatic multipolar interactions for the observed concentration quenching^{32,35}

3.2.3 Luminescence decay curve analysis. To gain more insight into the nature of the occupancy of Dy³⁺ ions and the energy transfer mechanism in the ZnO lattice, photoluminescence lifetime studies were performed. The luminescence decay curves corresponding to the ⁴F_{9/2} → ⁶H_{13/2} transition of Dy³⁺ ions with emission at 572 nm and excitation at 388 nm of Zn_{1-x}O:xDy³⁺ ($x = 0.04, 0.08, 0.12, 0.16, 0.2$) nanophosphors are shown in Fig. 11(a–e). The decay curve was found to be best fitted with a single-exponential function:

$$I(t) = I_0 \exp\left(-\frac{t}{\tau}\right) \quad (8)$$

where τ is the lifetime of the activator ion and I_0 is the initial emission intensity at $t = 0$ s.⁴⁵ The fitting by a single-exponential function marks the single-site occupancy of Dy³⁺ ions. The fitted lifetime values are given in Table 5. The lifetime was found to increase with the increase in Dy³⁺ content up to $x = 0.16$ at%, beyond that, a slight decrease was observed and is attributed to the nonradiative transitions between activator ions due to the shortened interionic distance between Dy³⁺ ions. This was also evidenced by the decrease in emission intensity at higher concentrations. The observed long decay time is attributed to the dopant ions entrenched at the core of the crystallite site.

3.2.4 CIE chromaticity coordinates. The color coordinates of ZnO:Dy³⁺ nanophosphors were evaluated using the 1931 CIE chromaticity coordinates function from the emission spectra observed with 388 nm excitation,^{46,47} and the corresponding CIE diagram is displayed in Fig. 12.

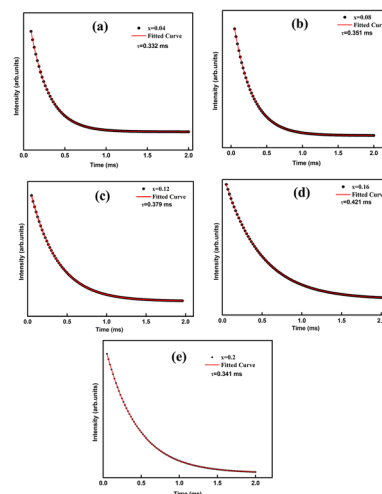


Fig. 11 Photoluminescence decay curves corresponding to the ⁴F_{9/2} → ⁶H_{13/2} transition ($\lambda_{em} = 572$ nm, $\lambda_{ex} = 388$ nm) of Dy³⁺ ions of ZnO:xDy³⁺ phosphors with different Dy³⁺ concentrations: (a) 0, (b) 0.04, (c) 0.08, (d) 0.12 (e) 0.16 and (f) 0.2 at%.

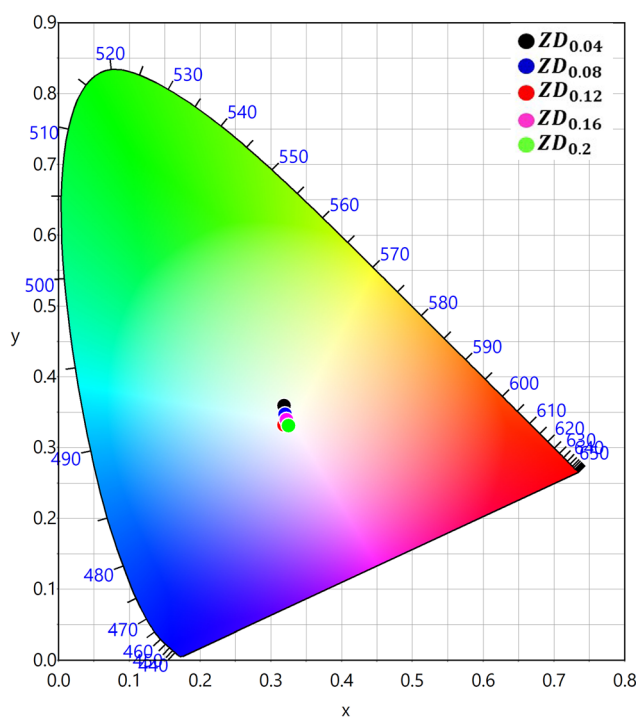


Fig. 12 CIE chromaticity diagram of ZnO:Dy³⁺ nanophosphors with varying Dy³⁺ content (0.04–0.2 at%).

The CIE chromaticity coordinates and correlated color temperature of ZnO:Dy³⁺ nanophosphors under excitation ($\lambda_{ex} = 388$ nm) for different Dy³⁺ ion concentrations are given in Table 3. The table indicates that ZnO:Dy³⁺ nanophosphors exhibit superior white luminescence coordinates that are extremely close to the National Television System Committee (NTSC) white-light emission and commercial pc-LED having

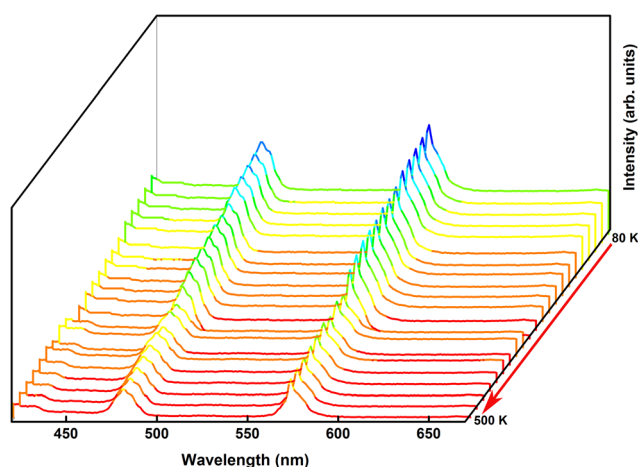
Table 3 Chromaticity coordinates and the correlated color temperature ZnO:Dy³⁺ nanophosphors under 388 nm excitation

Dy doping level (at %)	CIE coordinates		CCT (Kelvin)
	x	y	
Standard	0.333	0.333	5471
0.04	0.321 ± 0.0085	0.339 ± 0.0042	6028 ± 393.8
0.08	0.32 ± 0.0092	0.347 ± 0.0099	6047 ± 407.2
0.12	0.325 ± 0.0056	0.332 ± 0.0007	5854 ± 270.8
0.16	0.329 ± 0.00283	0.334 ± 0.0007	5657 ± 131.5
0.2	0.325 ± 0.0056	0.331 ± 0.0014	5856 ± 272.2

(0.310, 0.316) and (0.32, 0.32), respectively.⁴⁸ The calculated CCT values for Dy³⁺ ion-doped ZnO phosphors were found to vary between 5471 and 6047 K and fall in the cool-white region of the chromaticity diagram, which signifies the possibility of the application of the phosphor in WLEDs for outdoor illumination.⁴⁹ The higher value of CCT indicates better visual acuity and greater brightness perception as compared to lower values.^{48,49} These results indicate that the ZnO:Dy³⁺ nanophosphor can be considered a possible candidate for the fabrication of WLEDs based on NUV chips as the excitation source.

3.2.5 Temperature-dependent photoluminescence. The thermal stability of the phosphor materials is one of the key conditions for solid-state lighting applications. To understand the thermal behavior of the phosphors, the emission intensity of the phosphor with the optimum concentration, ZnO:0.16Dy³⁺ was monitored under 388 nm excitation at various temperatures from 80 K to 500 K (Fig. 13).

The emission spectra showed a slight variation in intensity with temperature in the range of 80–320 K. However, a fast decrease in intensity with the increase in temperature was observed above 320 K. The decrease in emission intensity can be ascribed to thermal quenching due to the increase in non-radiative transitions at elevated temperatures. Also, no change in the luminescence profile was noted at higher temperatures. The

**Fig. 13** Temperature-dependent emission spectra of ZnO: 0.16 Dy³⁺ nanophosphors at an excitation of 388 nm.

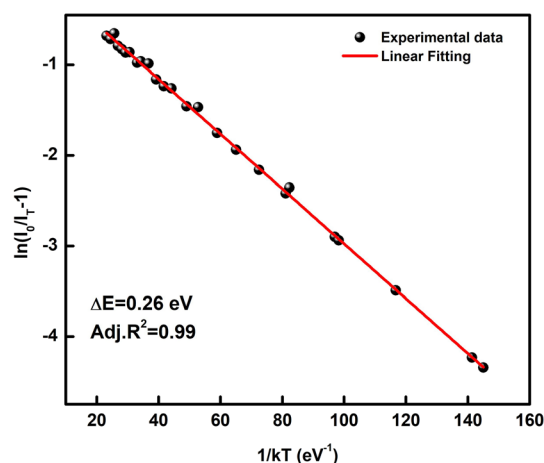
thermal stability of the phosphor was evaluated by calculating the activation energy based on the Arrhenius equation:^{50,51}

$$I_T = \frac{I_0}{1 + Ae^{-\Delta E/kT}} \quad (9)$$

where I_0 and I_T are luminescence intensities at room temperature and a temperature T ; $k = 8.617 \times 10^{-5}$ eV; K^{-1} is the Boltzmann constant; A is a constant, and ΔE is the activation energy. The thermal activation energy of the phosphor can be obtained from the $\frac{1}{kT}$ vs. $\ln\left(\frac{I_0}{I_T} - 1\right)$ plot and was found to be 0.26 eV (Fig. 14). The obtained higher thermal activation energy indicates better thermal stability for the phosphors.

3.3 Judd Ofelt analysis and radiative properties of ZnO:xDy³⁺ nanophosphors

Judd–Ofelt (J–O) analysis is a widely used theory to understand the spectroscopic and luminescence dynamics of lanthanide ions in crystals.^{51–54} The three J–O parameters Ω_λ ($\lambda = 2, 4$, and 6) are evaluated empirically from the absorption spectra and provide information about the structural environment and bonding between rare earth ions in the host lattice. J–O parameters are determined by fitting experimental line strength data with the theoretical value by utilizing the proportionality between the absorption and excitation spectra. The radiative parameters such as the spontaneous emission probabilities, the oscillator strength, and the radiative branching ratios between J -multiplets of RE ions can be easily estimated using J–O parameters.^{52,53} Luo *et al.*⁵⁵ developed a new method for evaluating the JO parameters of nanomaterials with low RE dopant concentration based on excitation spectra. Zhang *et al.*⁵⁶ proposed another method for calculating the J–O parameters of RE³⁺-doped powder based on the diffuse-reflection spectrum. In this route, the absorption cross-section spectrum was derived from the diffuse-reflection spectrum by taking the Kubelka–Munk function into account and by using the connection between the absorption cross section and the radiative

**Fig. 14** Linear fit of the Arrhenius equation of ZnO:0.16Dy³⁺ nanophosphors.

transition rate. Luo *et al.*⁵⁷ proposed a new method for evaluating J–O parameters and radiative parameters of trivalent rare earth ion-doped materials of any form, and in this route, the relation between the fluorescence decay values and the radiative transition rates was utilized. In this work, the J–O intensity parameters of ZnO:Dy³⁺ nanophosphors are determined from excitation spectra by adopting the method proposed by Luo *et al.*⁵⁵ The oscillator strength of absorption from an initial state (*J*) to the final state (*J'*) is given by the following:

$$f_{(J \rightarrow J')} = f_{ED} + f_{MD} = \frac{8\pi^2 m c \nu}{3 h e^2 n^2 (2J+1)} (\chi_{ED} S_{ED} + \chi_{MD} S_{MD}) \quad (10)$$

where *m* is the mass of the electron, *h* is Planck's constant, ν is the frequency of the excitation spectra, χ_{ED} and χ_{MD} are the correction factors of the refractive index of the medium in which the ion is embedded for ED and MD transitions, and are evaluated using $\chi_{ED} = \frac{n(n^2+1)^2}{9}$ and $\chi_{MD} = n^3$.^{55,58}

The excitation line strength for an electric dipole transition can be expressed in terms of $\Omega_{2,4,6}$ as follows:

$$S_{ED}^{Cal} = e^2 \sum_{\lambda=2,4,6} Q_{\lambda} |\langle \Psi_J \| U^{\lambda} \| \Psi_{J'} \rangle|^2 \quad (11)$$

where $|\langle \Psi_J \| U^{\lambda} \| \Psi_{J'} \rangle|^2$ represents the squared reduced matrix element of the irreducible tensor operator. The values of these matrix elements for Dy³⁺ are independent of the host material and have been reported by Carnell *et al.*⁵⁹ U^{λ} is related to the spin coupling and electron repulsion. The measured line strength can be determined from the observed excitation spectrum as follows:

$$S_{ED}^{Meas} = \frac{3hc(2J+1)}{8e^2\pi^3\lambda N_0} \frac{9n}{(n^2+2)^2} \Gamma_{ex} \quad (12)$$

where λ is the mean wavelength of the excitation spectra and N_0 is the concentration of Dy³⁺ ions. The refractive index (*n*) of this nanophosphor was determined by the reflection ellipsometry technique to be 2.24. The J–O parameters Ω_2 , Ω_4 , and Ω_6 are determined by least squares fitting of the experimental line strength data S_{ED}^{Cal} with the calculated line strength data S_{ED}^{Meas} . The root mean square deviation of experimental and calculated line strength values is determined as follows:

$$\Delta S_{rms} = \sqrt{\frac{\sum_{i=1}^N (S_{meas} - S_{cal})^2}{(N-3)}} \quad (13)$$

where *N* is the number of experimental spectral lines involved in the calculation. The J–O parameters Ω_2 , Ω_4 and Ω_6 calculated using the above relations are given in Table 4. From the table, the value of Ω_2 value increases with the Dy³⁺ ion concentration and it accounts for the increase in the asymmetry of the local environment of the luminescent ions. The observed trend of $\Omega_2 > \Omega_4 > \Omega_6$ indicates the stronger covalent nature of the bonding of Dy³⁺ ions and more asymmetry around the Dy³⁺ ions in the ZnO matrix. The obtained J–O parameters can be used to evaluate the radiative properties of the nanophosphor from the emission spectra.

Table 4 Judd–Ofelt intensity parameters (Ω_2 , Ω_4 , and Ω_6) and ΔS_{rms} for ZnO:xDy³⁺ (*x* = 0.04, 0.08, 0.12, 0.16, 0.20) nanophosphors

Sample	Ω_2 ($\times 10^{-20}$ cm ²)	Ω_4 ($\times 10^{-20}$ cm ²)	Ω_6 ($\times 10^{-20}$ cm ²)	ΔS_{rms} ($\times 10^{-21}$ cm ²)	Asymmetric ratio
ZD _{0.04}	0.81	0.124	0.0065	3.15	1.06
ZD _{0.08}	0.97	0.218	0.0104	2.23	1.16
ZD _{0.12}	1.61	0.471	0.0532	2.15	1.25
ZD _{0.16}	2.38	0.803	0.0564	1.47	1.37
ZD _{0.2}	1.97	0.689	0.0106	9.13	1.10

The electric dipole transition rate of ${}^4F_{9/2} \rightarrow {}^6H_J$ ($J = 15/2, 13/2$) is given by,

$$A_{9/2 \rightarrow J} = \frac{64\pi^4 \nu^3}{3h(2J+1)} e^2 \frac{n(n^2+2)^2}{9} \sum_{\lambda} \Omega_{\lambda} \left| \langle {}^4F_{9/2} \| U^{(\lambda)} \| {}^6H_J \rangle \right|^2 \quad (14)$$

The rate of the magnetic dipole transition, $A_{9/2 \rightarrow 15/2}$, can be evaluated by taking the ratio of the integrated emission intensity, which is directly proportional to the transition rate of each energy level:

$$\frac{\int I_{9/2 \rightarrow J}}{\int I_{9/2 \rightarrow 15/2}} = \frac{A_{9/2 \rightarrow J}}{A_{9/2 \rightarrow 15/2}} \quad (15)$$

Total radiative transition probability A_R is the sum of all electric and magnetic dipole transition probabilities.

$$A_R = \sum_J A_{9/2 \rightarrow J} \quad (16)$$

where $J = 15/2, 13/2$ and $11/2$.⁶⁰ The radiative lifetime τ_{rad} of the emitting state ${}^4F_{9/2}$ is related to the spontaneous emission probabilities for all transitions from this state to the low-lying 6H_J states:

$$\tau_{rad} = \frac{1}{\sum_J A_{R(J \rightarrow J')}} \quad (17)$$

Quantum efficiency (η) is another important parameter and is defined as the ratio of the observed lifetime (τ_{obs}) to the radiative lifetime (τ_{rad}) and is given by

$$\eta = \frac{\tau_{obs}}{\tau_{rad}} \quad (18)$$

The fluorescence branching ratio, which is a measure of the relative contribution of each transition from the excited state to a lower state, is determined as follows:

$$\beta_{9/2 \rightarrow J} = \frac{A_{9/2 \rightarrow J}}{\sum_J A_{9/2 \rightarrow J}} \quad (19)$$

where $J = 15/2, 13/2$ and $11/2$. The stimulated emission cross-section for the transition ${}^4F_{9/2} \rightarrow {}^6H_J$ is related to the radiative transition probability:

$$\sigma_{9/2 \rightarrow J} = \frac{\lambda_p^4 A_{9/2 \rightarrow J}}{8\pi c n^2 \Delta \lambda_{eff}} \quad (20)$$

Table 5 Transition rates (A_R , A_{NR} and A_T), lifetimes (τ_{rad} and τ_{obs}), quantum efficiency (η), branching ratios (β) and stimulated emission cross sections (σ) of the transitions ${}^4F_{9/2} \rightarrow {}^6H_{15/2}$, ${}^4F_{9/2} \rightarrow {}^6H_{13/2}$, and ${}^4F_{9/2} \rightarrow {}^6H_{11/2}$ for ZnO:Dy³⁺ nanophosphors

Radiative parameter	ZD _{0.04}	ZD _{0.08}	ZD _{0.12}	ZD _{0.16}	ZD _{0.2}
A_R (s ⁻¹)	1974	2190	2375	2210	2580
A_{NR} (s ⁻¹)	1038	659	264	165	353
A_T (s ⁻¹)	3012	2849	2639	2375	2933
τ_{rad} (ms)	0.506	0.456	0.421	0.452	0.388
τ_{obs} (ms)	0.332	0.351	0.379	0.421	0.341
η (%)	66	77	90	93	87
$\beta_{9/2 \rightarrow 15/2}$ (%)	6.12	5.54	5.86	6.23	5.98
$\beta_{9/2 \rightarrow 13/2}$ (%)	73.15	74.23	75.03	76.12	73.92
$\beta_{9/2 \rightarrow 11/2}$ (%)	16.32	16.01	15.94	15.74	15.82
$\sigma_{9/2 \rightarrow 15/2}$ ($\times 10^{-22}$ cm ²)	4.09	4.16	4.32	5.58	5.33
$\sigma_{9/2 \rightarrow 13/2}$ ($\times 10^{-21}$ cm ²)	3.23	3.42	3.67	3.91	3.44
$\sigma_{9/2 \rightarrow 11/2}$ ($\times 10^{-22}$ cm ²)	5.42	5.57	6.18	7.43	6.61

where λ_p is the wavelength of the emission peak and $\Delta\lambda_{eff}$ is the effective line width of the emission band. The obtained values of radiative parameters are summarized in Table 5.

The quantum efficiency and lifetime values were found to increase with an increase in Dy³⁺ concentration, which suggests that Dy³⁺ incorporation reduces the non-radiative relaxation mechanism. Also, the highest quantum efficiency of 93% was obtained for ZnO:Dy³⁺ nanophosphors with optimum Dy³⁺ content (0.16 at%). The high value of the branching ratio and stimulated emission cross-section for the ${}^4F_{9/2} \rightarrow {}^6H_{13/2}$ transition indicates that the yellow emission band is the efficient transition in this ZnO:Dy³⁺ nanophosphor and has the potential to be used for the fabrication of WLED's.

4. Conclusions

Single-phase white-light emitting ZnO:Dy³⁺ nanophosphors with varying Dy content (0.04–0.2 at%) were successfully synthesized *via* a sonochemical method. X-ray diffraction and Raman spectroscopic analysis indicated the formation of hexagonal wurtzite-structured ZnO with preferential growth along the (101) crystal plane. Scanning electron micrographs indicated the formation of ribbon-shaped nanostructures. The X-ray photoelectron spectra revealed the existence of only trivalent dysprosium ions in the ZnO lattice. Strong yellow (572 nm), blue (480 nm), and red (635 nm) emission bands were observed in the visible region upon efficient excitation by near-UV light of wavelength 388 nm. The optimum incorporation of Dy³⁺ (0.16 at%) in the ZnO:Dy³⁺ nanophosphor enhanced the intensity of emission along with an increase in the asymmetric ratio from 1 to 1.37. The single-exponential nature of the luminescence decay curves indicated the substitution of the Dy³⁺ ions at unique crystallite sites. The thermal activation energy of 0.26 eV obtained for optimum ZnO:Dy³⁺ nanophosphors suggests substantial stability against thermal quenching due to the cross-over process. The Judd–Ofelt intensity parameters were evaluated from the excitation spectra of the ZnO:Dy³⁺ nanophosphor. The radiative properties of these

nanophosphors were quantitatively evaluated and a maximum quantum efficiency of 93% was obtained in the optimum case. The high values of emission cross-section and branching ratio for the ${}^4F_{9/2} \rightarrow {}^6H_{13/2}$ transition indicated that the yellow emission band is the efficient transition in this ZnO:Dy³⁺ nanophosphor. All the results indicate that the ZnO:Dy³⁺ nanophosphor could be used as a practical potential luminescent material for NUV-based W-LED applications.

Author contributions

The manuscript was written through contributions of all authors. All authors have given approval to the final version of the manuscript. K.G. Gopchandran designed the work; Raji R. executed the experimental work and wrote the manuscript in discussion with Jyothi G and Sajesh Sasidharan.

Conflicts of interest

There are no conflicts to declare.

Acknowledgements

The authors acknowledge the Central Laboratory for Instrumentation and Facilitation (CLIF) of the University of Kerala for the instrumentation support.

References

- E. F. Schubert and J. K. Kim, *Science*, 2005, **308**(5726), 1274–1278.
- H. Dong, S. R. Du, X. Y. Zheng, G. M. Lyu, L. D. Sun, L. D. Li, P. Z. Zhang, C. Zhang and C. H. Yan, *Chem. Rev.*, 2015, **115**, 10725–10815.
- Y. Liu, D. Tu, H. Zhu and X. Chen, *Chem. Soc. Rev.*, 2013, **42**(16), 6924–6958.
- P. Pust, P. J. Schmidt and W. Schnick, *Nat. Mater.*, 2015, **14**(5), 454–458.
- G. Liu and B. Jacquier, *Spectroscopic Properties of Rare Earths in Optical Materials*, Springer, Berlin, 2005.
- G. H. Dieke, *Spectra and Energy Levels of Rare Earth Ions in Crystals*, Wiley, New York, 1968.
- G. Blasse and B. C. Grabmaier, *Luminescent Materials*, Springer-Verlag, Berlin, 1994.
- S. Hufner, *Optical Spectra of Transparent Rare Earth Compounds*, Academic Press, New York, 1978.
- U. Ozgur, Y. I. Alivov, C. Liu, A. Teke, M. A. Reshchikov, S. Dogan, V. Avrutin, S. J. Cho and H. Morkoc, *J. Appl. Phys.*, 2005, **98**, 041301–041404.
- A. Janotti and C. G. Van de Walle, *Rep. Prog. Phys.*, 2009, **72**, 126501–126530.

- 11 H. Morkoc and U. Ozgur, *Zinc oxide: Fundamentals, materials and device technology*, Wiley-VCH Verlag GmbH & Co, KGaH, Germany, 2009.
- 12 P. A. Rodnyi and I. V. Khodyuk, *Opt. Spectrosc.*, 2011, **111**, 814–824.
- 13 A. R. Gheisi, C. Neygandhi, A. K. Sternig, E. Carrasco, H. Marbach, D. Thomelec and O. Diwald, *Phys. Chem. Chem. Phys.*, 2014, **16**, 23922.
- 14 B. D. Yuhas, D. O. Zitoun, P. J. Pauzauskie, R. He and P. Yang, *Angew. Chem.*, 2006, **118**, 434–437.
- 15 C. X. Xu, X. W. Sun, X. H. Zhang, L. Ke and S. J. Chua, *Nanotechnology*, 2004, **15**, 856–861.
- 16 A. Bindhu, J. I. Naseemabeevi and S. Ganesanpotti, *Dalton Trans.*, 2023, **52**(33), 11705–11715.
- 17 P. Vasudevan, V. Vidyadharan, S. M. Simon and N. V. Unnikrishnan, *J. Sci.: Adv. Mater. Devices*, 2020, **5**(2), 242–249.
- 18 W. Yuan, R. Pang, S. Wang, T. Tan, C. Li, C. Wang and H. Zhang, *Light: Sci. Appl.*, 2022, **11**(1), 184.
- 19 T. Samanta, N. S. M. Viswanath, S. W. Jang, J. W. Min, H. B. Cho, J. H. Han and W. B. Im, *Adv. Opt. Mater.*, 2023, **11**(9), 2202744.
- 20 S. Dutta, S. Som and S. K. Sharma, *RSC Adv.*, 2015, **5**(10), 7380–7387.
- 21 M. A. Almessiere, Y. Slimani, H. Güngüneş, A. D. Korkmaz, T. Zubar, S. Trukhanov, A. Trukhanov, A. Manikandan, F. Alahmari and A. Baykal, *ACS Omega*, 2021, **6**(15), 10266–10280.
- 22 P. Kumar, R. Singh and P. C. Pandey, *J. Appl. Phys.*, 2018, **123**(5), 054502.
- 23 Y. Q. Jia, *J. Solid State Chem.*, 1991, **95**(1), 184–187.
- 24 B. D. Cullity, *Elements of X-ray Diffraction*, Addison-Wesley Publishing Company Inc., Massachusetts, USA, 1956.
- 25 R. Raji and K. G. Gopchandran, *J. Phys. Chem. Solids*, 2018, **113**, 39–49.
- 26 J. M. Calleja and M. Cardona, *Phys. Rev. B: Solid State*, 1977, **16**, 3753.
- 27 T. C. Damen, S. P. S. Porto and B. Tell, *Phys. Rev.*, 1966, **142**, 570.
- 28 M. Rajalakshmi, A. K. Arora, B. S. Bendra and S. Mahamuni, *J. Appl. Phys.*, 2000, **87**, 2445–2448.
- 29 F. J. Manjon, B. Mari, J. Serrano and A. H. Romero, *J. Appl. Phys.*, 2005, **97**, 053516–053250.
- 30 C. Jayachandriah, K. S. Kumar, G. Krishnaiah and N. M. Rao, *J. Alloys Compd.*, 2015, **623**, 248–254.
- 31 G. Amira, B. Chaker and B. E. Habib, *Spectrochim. Acta, Part A*, 2017, **177**, 164–169.
- 32 R. Raji, R. A. Kumar and K. G. Gopchandran, *J. Lumin.*, 2019, **205**, 179–189.
- 33 D. Barreca, A. Gasparotto, A. Milanov, E. Tondello, A. Devi and R. A. Fischer, *Surf. Sci. Spectra*, 2007, **14**(1), 52–59.
- 34 S. Sasidharan, G. Jyothi, S. Sameera and K. G. Gopchandran, *J. Solid State Chem.*, 2020, **288**, 121449.
- 35 M. Manhas, V. Kumar, O. M. Ntwaeaborwa and H. C. Swart, *Ceram. Int.*, 2016, **42**(5), 5743–5753.
- 36 A. E. Morales, E. S. Mora and U. Pal, *Rev. Mex. Fis.*, 2007, **53**(5), 18–22.
- 37 M. Luo, X. Sha, B. Chen, X. Zhang, H. Yu, X. Li, J. Zhang, S. Xu, Y. Cao, Y. Wang and X. Wang, *J. Am. Ceram. Soc.*, 2022, **10**, 3353–3363.
- 38 E. Burstein, *Phys. Rev.*, 1954, **93**(3), 632.
- 39 Z. M. Gibbs, A. LaLonde and G. J. Snyder, *New J. Phys.*, 2013, **15**, 075020.
- 40 V. R. Akshay, B. Arun, G. Mandal and M. Vasundhara, *New J. Chem.*, 2019, **43**(37), 14786–14799.
- 41 M. K. Musembi, F. B. Dejene and I. Ahemen, *OSA Continuum*, 2020, **3**(9), 2332–2346.
- 42 D. Xu, Z. Yang, J. Sun, X. Gao and J. Du, *J. Mater. Sci.: Mater. Electron.*, 2016, **27**, 8370–8377.
- 43 G. Jyothi, L. S. Kumari and K. G. Gopchandran, *Ceram. Int.*, 2017, **43**, 12044–12056.
- 44 G. Blasse, *Phys. Lett.*, 1968, **28**, 444–445.
- 45 R. G. A. Kumar, S. Hata, K. Ikeda and K. G. Gopchandran, *RSC Adv.*, 2016, **6**, 67295–67307.
- 46 R. W. G. Hunt, *Measuring Colour: Applied Science and Industrial Technology*, Second ed., Ellis Horwood, New York, 1991.
- 47 C. S. McCamy, *Color Res. Appl.*, 1992, **17**, 142–144.
- 48 M. R. N. Soares, M. J. Soares, A. J. S. Fernandes, L. Rino, F. M. Costa and T. Monteiro, *J. Mater. Chem.*, 2011, **21**(39), 15262–15265.
- 49 A. K. Vishwakarma, K. Jha, M. Jayasimhadri, B. Sivaiah, B. Gahtori and D. Haranath, *Dalton Trans.*, 2015, **44**(39), 17166–17174.
- 50 A. Bindhu, J. I. Naseemabeevi and S. Ganesanpotti, *J. Sci.: Adv. Mater. Devices*, 2022, **7**(2), 100444.
- 51 S. Sasidharan, G. Jyothi and K. G. Gopchandran, *J. Sci.: Adv. Mater. Devices*, 2022, **7**(1), 100400.
- 52 B. Judd, *Phys. Rev.*, 1962, **127**, 750.
- 53 G. S. Ofelt, *J. Chem. Phys.*, 1962, **37**, 511–520.
- 54 Y. Tian, B. Chen, R. Hua, J. Sun, L. Cheng, H. Zhong, X. Li, J. Zhang, Y. Zheng, T. Yu and L. Huang, *J. Appl. Phys.*, 2011, **109**(5), 053511.
- 55 W. Luo, J. Liao, R. Li and X. Chen, *Phys. Chem. Chem. Phys.*, 2010, **12**(13), 3276–3282.
- 56 Y. Zhang, B. Chen, S. Xu, X. Li, J. Zhang, J. Sun, X. Zhang, H. Xia and R. Hua, *Phys. Chem. Chem. Phys.*, 2019, **21**(20), 10840–10845.
- 57 M. Luo, B. Chen, X. Li, J. Zhang, S. Xu, X. Zhang, Y. Cao, J. Sun, Y. Zhang, X. Wang and Y. Zhang, *Phys. Chem. Chem. Phys.*, 2020, **22**(43), 25177–25183.
- 58 C. Shivakumara, R. Saraf and P. Halappa, *Dyes Pigm.*, 2016, **126**, 154–164.
- 59 W. T. Carnall, H. M. Crosswhite and H. Crosswhite, *Energy level structure and transition probabilities in the spectra of the trivalent lanthanides in LaF₃*, (No. ANL-78-XX-95), Argonne Natl., Lab. Report, Argonne, IL, USA, 1978.
- 60 K. Li, M. Dai, Z. Fu, Z. Wang, H. Xu and R. Wang, *Inorg. Chem. Front.*, 2024, **11**(1), 172–185.